Impact Characteristics in Fused Silica for Various Projectile Velocities

ROBERT E. FLAHERTY*
NASA Manned Spacecraft Center, Houston, Texas

A special technique has been developed for examination of crater cross sections in fused silica targets. Photomicrographs show that low-velocity impact craters, when viewed with bottom lighting, have approximately 75% of the crater area blacked out because of fractures that totally reflect the light, but for craters from hypervelocity impacts (5 km/sec and more), this blacked out area approximates 10%. The ratios of the crater diameter to crater depth (deepest fissure) for low-velocity and hypervelocity impacts average 2 and 7, respectively. The hypervelocity impacts exhibit a well-defined central region of pulverized glass surrounded by a large, smooth conchoidal chip-out, and at velocities above 10 km/sec, this central area shows signs of hydrodynamic flow. The depth predicted by use of the Manned Spacecraft Center glass-penetration equation is about one-half the actual depth of the deepest fissure.

Introduction

THE Meteroid Sciences Branch of the Manned Spacecraft Center (MSC) is conducting a meteoroid impact experiment using the external surfaces of the fused silica windows of the Apollo command module. The windows are microscopically scanned before and after flight to determine the size and number of surface imperfections. Because no existing publications described impact craters in fused silica targets in sufficient detail to permit classification of impacting projectiles as to high or low velocity, the experimental program described herein was undertaken.

Velocity Ranges and Method of Target Analysis

The experimental data were obtained by impacting fused silica targets with projectiles in four velocity ranges. The first range, 0.15–1.0 km/sec, was obtained by using a specially designed, vertically mounted 0.44-magnum gun. The gun propelled sabot-supported particles ranging from 50 μ to 0.635 cm in. diam. In flight, the particles interrupted a light beam that triggered an image-intensifier camera system and a time-of-flight clock. Two such triggering stations were used to measure the velocity and integrity of the particle. The second velocity range, 1.0–2.4 km/sec, was achieved using both a 30–06 powder gun and a miniature light gas gun that was purposely slowed down. Both facilities used an electronically controlled system of image-intensifier cameras to measure particle velocity. A second light-gas gun provided the third velocity range, 6.0–7.5 km/sec; the photographic technique previously described was used to determine velocity. In addition, impacts of small particles with indicated velocities of as much as 10 km/sec were achieved by using a plasma-drag accelerator facility at the Martin Company.

Historically, impact-crater damage in glass has been described only in terms of depth from the original target surface and diameter of the surface area damaged. This system of description provided no information on internal damage, such as chipped and pulverized glass below the crater, and fissures that extend below the pulverized zone. Therefore, a special technique for examination has been developed. The glass target is sectioned near the crater, and the resulting edge is carefully polished to permit undistorted microscopic observation of the crater through the glass. The distance from the crater to the section plane is dependent upon the magnification desired, and the corrected optical path length has to be within the focal distance of the microscopic objective lens. When bottom lighting is used, a microscopic image of the impact crater is formed by proper positioning of the target, which results in a cross-sectional view of the pulverized zone of the crater and in a shadowgraph of the internal cracks and fissures. Various cross sections are observed by focusing at different planes through the crater. The fissures appear black or various shades of gray because of the percentage of light reflection at the boundary interface. As the focusing plane is changed, the image appears as a translucent veil waving in a light breeze, and the image varies from opaque to transparent as the fissure width changes from fractional to multiple wavelengths. (If monochromatic light is used, fissures can be detected that are separations in the glass a fraction of the illuminating wavelength wide.) For small craters, it is often necessary to tilt the target to obtain the best image. This tilting results in a reflected image.

The photomicrographs obtained are studied to determine velocity and energy dependent characteristics and the depth of the deepest fissure. This depth is compared to the depth predicted by

$$P_c = 0.53 d_p^{1.06} \rho_p^{1/2} V^{2/3} \quad (1)$$

where P_c = calculated penetration depth measured from the top surface in cm, d_p = projectile diameter in cm, ρ_p = projectile density in g/cm^3, and V = projectile velocity in km/sec. This is the basic penetration equation for impacts in to semi-infinite metal targets,[1] which has been modified by a scale factor of $d_p^{1.06}$ as discussed in Ref. 2, where the constants have been determined by laboratory impact testing.

Data Description

Low Velocity

The data of the low-velocity series ($V < 1.0$ km/sec) are grouped in Table 1 in order of increasing energy for each of three impacting projectiles: 1-mm Pyrex, 1.58-mm Pyrex, and 1-mm aluminum. In the impacted targets, the amount of chipping visible from the top surface increased with projectile energy. All craters in this series, when viewed with bottom lighting (i.e., with transmitted light), had approximately 75% of the total damaged area blacked-out because of total reflection. This effect can be expected for all types of low-energy-impact damage, such as chips caused by tools (Fig. 1), scratches, and mishandling. The surface features were very

Presented as Paper 69-367 at the AIAA Hypervelocity Impact Conference, Cincinnati, Ohio, April 30–May 2, 1969; submitted May 15, 1969; revision received November 12, 1969.

* Aerospace Technologist, Meteoroid Sciences Branch, Space Physics Division.

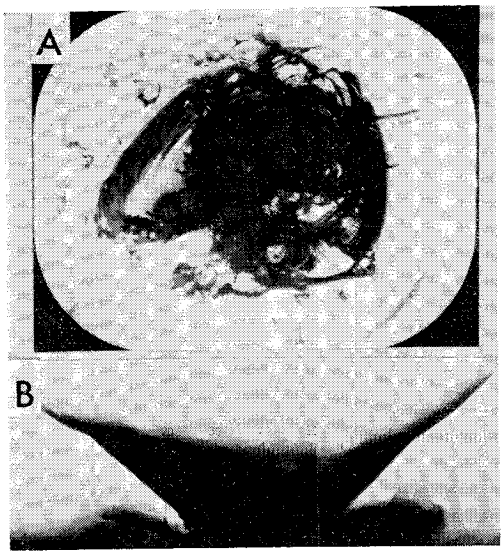

Fig. 1 A 1.1-mm-deep, 3-mm-diam crater caused by striking fused silica with a center punch: A) top view with bottom lighting; B) cross-sectional view with bottom lighting. (Note in all cross section views the bottom of the microphotograph shows the top surface of the glass.) For this crater the subsurface diameter is larger than the top surface diameter.

rough and filled with chipped and shattered glass. Frequently, a top surface spallation of a rough conchoidal chip-out was observed. The typical effects of these low-energy impacts are shown in Figs. 1 and 2. The surface damage diameter d_c divided by the depth of the deepest fissure P for the low-velocity impacts tested averaged 1.72, with an average deviation of 0.33.

The over-all crater size and depth were strongly dependent upon the size and hardness of the impacting particle.

The cross-sectional views of these craters revealed an increase in the complexity and number of fissures structures as the impact energy increased. The typical low-energy impact effect is shown in Fig. 1. The crater cross section is described as a conical fissure structures. With increased energy, the conical fissure structures developed into the more complex petaloid structures shown in Fig. 2. The number of petaloid structures increased rapidly with energy until the individual structures became obscured by total reflection and until horizontal separations parallel to the target surface appeared (see Fig. 2b). The development and growth of these horizontal

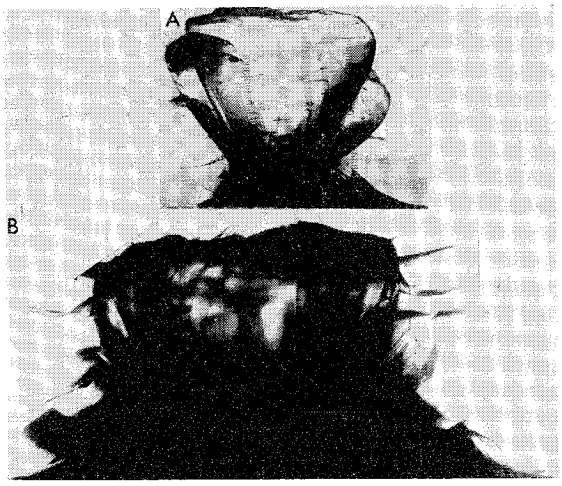

Fig. 2 Cross-sectional views of craters produced by Pyrex projectiles at low velocity: A) d_p = 1 mm, V = 303 m/sec; B) d_p = 1.58 mm, V = 496 m/sec.

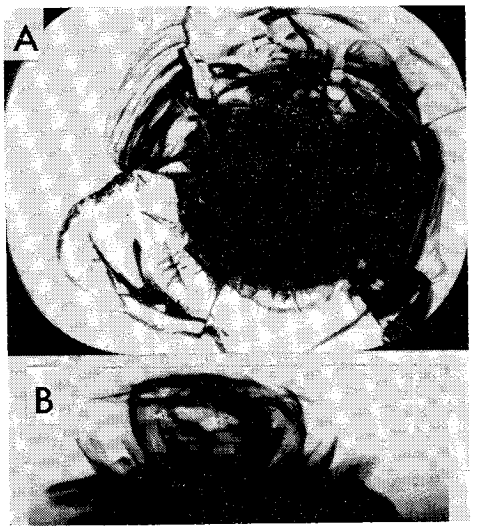

Fig. 3 A 1.03-mm-deep by 2.4-mm-diam crater produced by a 0.396-mm-diam sapphire projectile at 1.0 km/sec: A) top view with bottom lighting; B) cross-sectional view.

separations marked a transition in the crater-morphology vs velocity description, as discussed in the following section.

Midvelocity

The projectiles used in the midvelocity series (1.0–2.4 km/sec; see Table 1) were 0.396-mm-diam sapphire spheres. This projectile material was required because Pyrex and aluminum projectiles did not survive the launch acceleration. The target surfaces, when viewed with bottom lighting, had about 75% of the total damaged area blacked-out by total re-

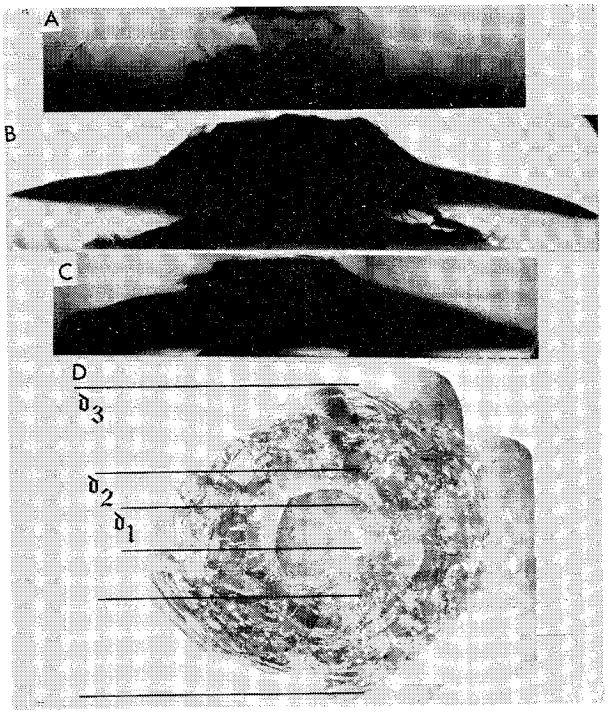

Fig. 4 Craters produced by 0.396-mm-diam sapphire projectiles at midvelocity: A) cross section; V = 1.68 km/sec, P = 1.23 mm, d_c = 5 mm; B) cross section; V = 2.25 km/sec, P = 1.6 mm, d_c = 6.6 mm; C) cross section; V = 2.4 km/sec, P = 1.7 mm, d_c = 7 mm; D) top view with bottom lighting of same crater as part C; region d_1 includes the dimpled area; d_2, the pulverized zone; and d_3, the rough chip-out zone.

Table 1 Projectile and crater data at three velocity ranges

Projectile							Crater			Calculations
d_p, mm	Material	Mass, g	ρ_p, g/cm^3	V, m/sec	$mV^2/2$, g-m^2/sec^2	mV, g-m/sec	d_c, mm	P, mm	d_c/P	Calculated depth, mm P_c
					Low velocity					
1	Pyrex	1.17×10^{-3}	2.23	170	16.9	02.0	1.6	0.82	1.95	No equations known to estimate depth for low or mid-velocity craters
				250[a]	36.5	0.29	2.1	2.1	1.0	
				303	53.7	0.35	2.7	2.23	1.2	
1.58	Pyrex	4.69×10^{-3}	2.23	184	79.4	0.86	4.1	2.4	1.7	
				299	210	1.40	6.6	3.3	2.0	
				496	576	2.32	7.8	3.4	2.29	
1	Aluminum	1.41×10^{-3}	2.7	320	72.2	0.45	1.6	0.83	1.92	
				517	188	0.72	3.1	1.64	1.89	
				680	326	0.96	2.83	2.26	1.26	
					Midvelocity					
0.396	Sapphire	1.34×10^{-4}	4.1	1000	67	0.13	2.4	1.03	1.98	
				1680	189	0.22	5.0	1.23	4.05	
				2250	339	0.30	6.6	1.61	4.1	
				2400	386	0.32	7.0	1.70	4.35	
0.396	Tungsten carbide	4.9×10^{-4}	15.6	2860	2512	1.75	17	3.23	5.26	
					Hypervelocity					
0.396	Pyrex	7.3×10^{-5}	2.23	6360	1470	0.46	13	1.82	7.1	0.89
				6800	1680	0.50	15	1.89	8.2	0.930
				6840	1700	0.50	16	1.95	8.2	0.936
0.396	Pyrex	7.3×10^{-5}	2.23	6900	1737	0.50	14	1.91	7.3	0.941
				7280	1934	0.53	13	1.77	7.3	0.975
				7480	2042	0.55	15	1.96	7.65	0.993
0.20	Pyrex	9.3×10^{-6}	2.23	6640	205	0.06	9.8	1.7	5.76	
0.20	Glass bead		2.2				0.22	0.03	7.3	
0.06[b]	Glass bead		2.2				0.12	0.09	1.34	
							0.19	0.14	1.36	
							0.32	0.07	4.77	
							1.5			

[a] Estimated. [b] Size of launched projectile, which fragmented at launch.

flection, as did the low-velocity series. As the projectile velocity increased, this percentage gradually decreased to ~40% at 2.25 km/sec.

The cross-sectional views of these craters revealed a transition in crater morphology beginning at a velocity between 1.0 and 1.68 km/sec and continuing to 2.4 km/sec. The crater (1.0-km/sec impact) shown in Fig. 3 exhibits multiple petaloid structures, and the crater (1.68-km/sec impact) shown in Fig. 4a exhibits a diameter increase by a factor of 2, horizontal separation, and numerous petaloid structures. At 2.25 km/sec (Fig. 4b) the number of petaloid structures had increased to such an extent that the cross section was opaque and the horizontal separation had extended beyond the surface diameter. This structural degradation marked the beginning at a spallation such as that shown in Fig. 4c. The surfaces of these craters (e.g., Fig. 4d) exhibited several features different from those of the low-velocity series. The point of impact had a slight dimple of diameter d_1, 2 to 3 times the projectile diameter d_p, and the depth of the dimple increased with projectile velocity V. The dimple was surrounded by a pulverized zone of diameter d_2, 5–8 times d_p, and the zone was, in turn, surrounded by rough chip-out of diameter D_3, 15–20 times d_p (D_3 was highly dependent upon V). Separations that had not been spalled off were often visible below the surface.

The crater diameter-to-depth ratio for the three impacts in the midvelocity range averaged 4.16, with an average deviation of 0.12 at velocities between 1.0 and 2.4 km/sec.

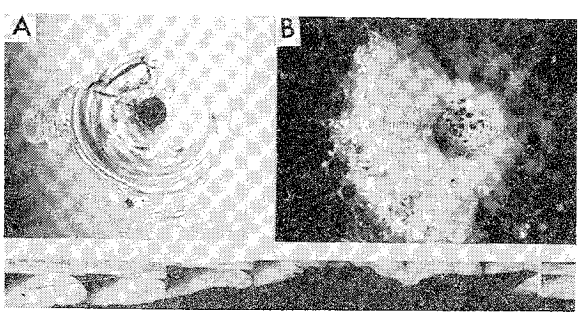

Fig. 5 A 1.9-mm-deep by 14-mm-diam crater produced by 0.396-mm-diam Pyrex projectile at 6.9 km/sec: A) top view, bottom lighted; B) top view, central area; bottom strip is cross-sectional view (enlarged mosaic).

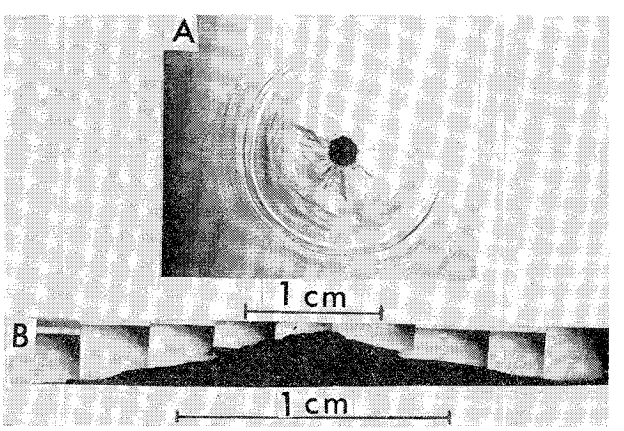

Fig. 6 An 2.0-mm-deep by 20-mm-diam crater produced by a 0.396-mm-diam Pyrex projectile on a cold-soaked target at 6.84 km/sec: A) top view, bottom lighted; B) cross-sectional view (enlarged mosaic).

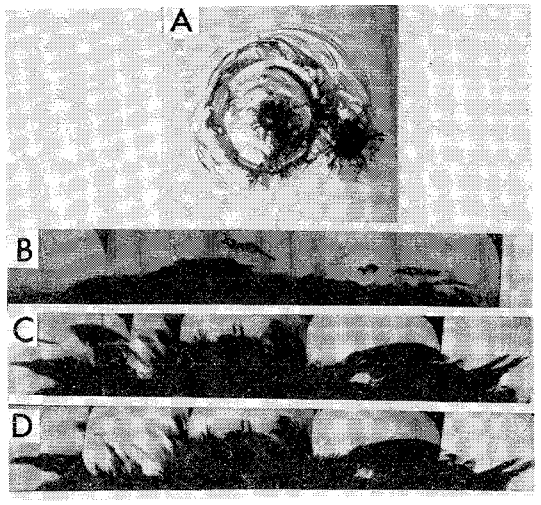

Fig. 7 Craters produced by multiple 0.20-mm-diam Pyrex projectiles at 6.87 km/sec: A) top view, bottom lighted (major crater is 2.18 mm deep and 12 mm in diameter); B) cross-sectional view 1 day after impact; C) cross section 1 week after impact; D) cross section 3 weeks after impact and after two thermal shocks.

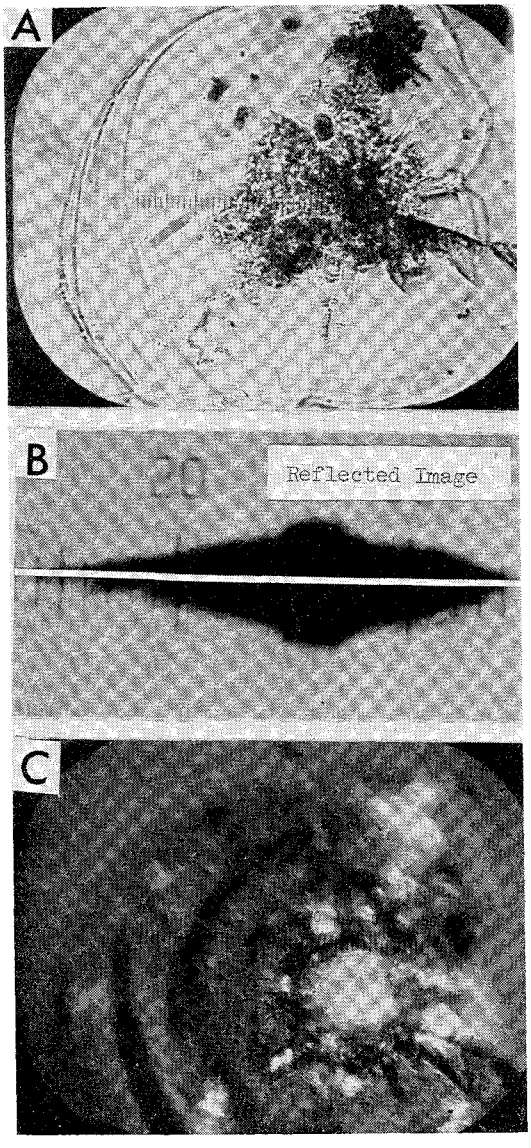

Fig. 8 A 0.03-mm-deep by 0.22-mm-diam crater produced by fragments from 0.20-mm-diam glass bead projectiles at unknown velocity: A) top view, bottom lighting; B) cross-sectional view (note reflected image); C) top view, top lighting.

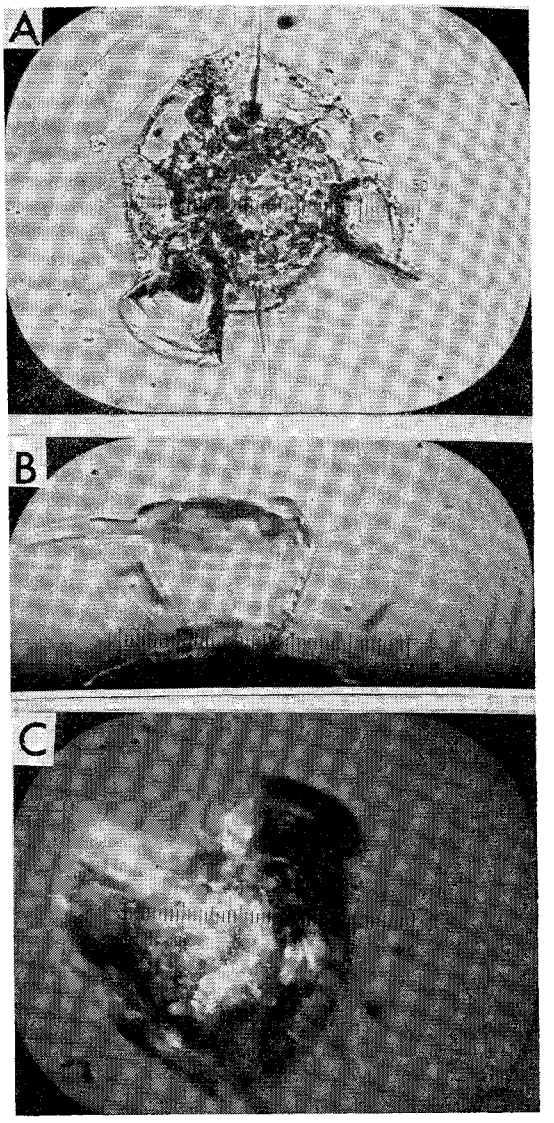

Fig. 9 A 0.12-mm-deep, 0.09-mm-diam crater produced by a fragment of 0.06-mm-diam glass bead projectile at unknown velocity: A) top view, bottom lighting; B) cross-sectional view; C) top view, top lighting.

Hypervelocity

The projectiles used for $6.0 \leq V \leq 7.5$ km/sec were 0.396-mm-diam, precision-ground Pyrex spheres. The crater surfaces, when viewed with bottom lighting, had less than 10% of the total damaged area blacked-out because of total reflection (Fig. 5a). The central zone of Fig. 5b (a 6.9 km/sec impact) consisted of pylverized glass that was generally 4 to 6 times d_p, and was often raised above the surrounding chipped area like a flat topped dome. The top of the dome shown in Fig. 5b was covered with a compacted, powdery glass with a depression at the point of impact. Such depressions were usually 2–3 times d_p. At $V \geq 6.9$ km/sec, the powdery layer is spalled off. This pulverized zone was surrounded by two concentric rings of chip-out. The inner ring, composed of a generally rough chip-out, was distinguishable in all top views by the darkening and more complex line structure adjacent to the dark central area. This area was, in turn, surrounded by a ring of generally smooth conchoidal chip-out that had a very rough and jagged external perimeter which marked the maximum area of target damage. The boundary between these areas is visible in all top-view photo-micrographs pertinent to this velocity range. The cross-sectional views of these craters revealed a generally smooth profile with a few scattered fis-

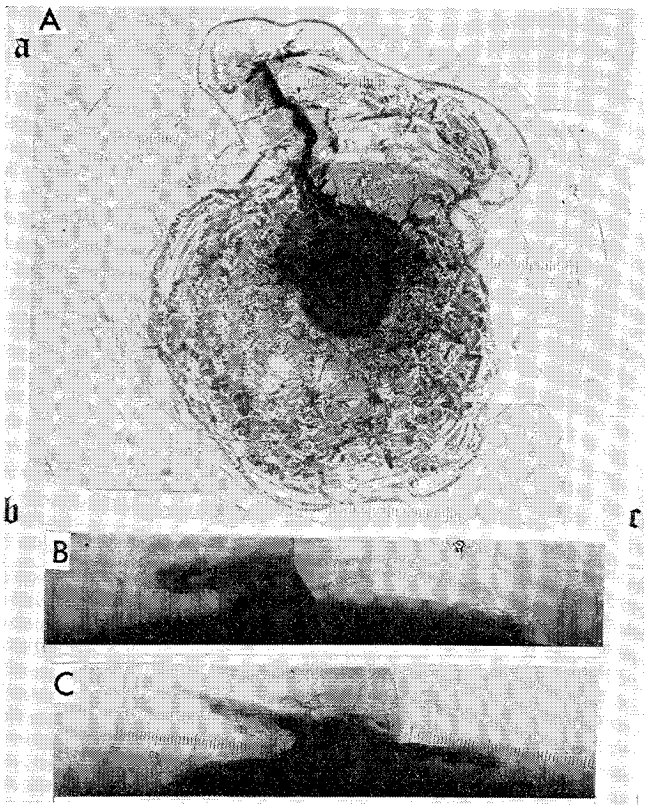

Fig. 10 A 0.33-mm-deep, 1.3-mm-diam meteoroid crater discovered on a Mercury 9 spacecraft window: A) top view, bottom lighting; B) cross-sectional view from plane a to plane b; C) cross-section from plane b to plane c, orthoganal to part (b).

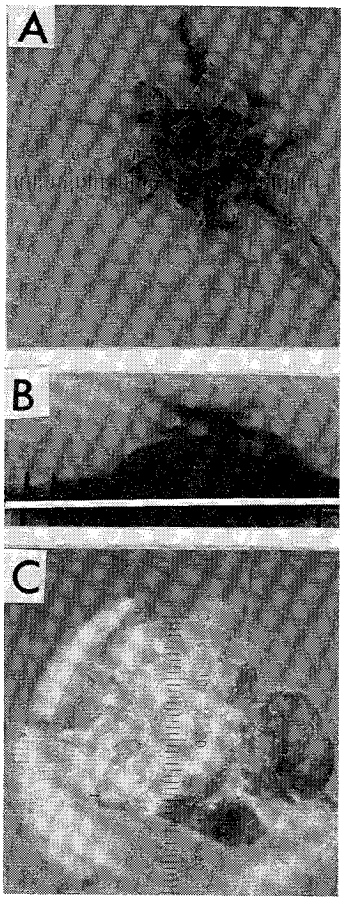

Fig. 11 Crater discovered on a Gemini V spacecraft window, 0.012 mm deep and 0.110 mm in diameter: A) top view bottom lighting; B) cross-sectional view; C) top view top lighting.

sures. Several crater cross sections revealed subsurface separation that had not been spalled off.

In an attempt to simulate the cold conditions of space, the target shown in Fig. 6 was soaked in liquid nitrogen for 30 min prior to impact. A thermocouple mounted on the rear surface of the target recorded −150°F at the time of impact. No apparent change was observed in the cross-sectional view where an extremely smooth conchoidal chip-out was obtained.

The multiple impact shown in Figs. 7a and 7b revealed an appreciable increase in crater size as the result of stress relief for approximately 1 week (Fig. 7c); 2 weeks later, the effects of entry heating on this target were investigated. Two thermal shocks had no apparent effect on the crater morphology (Fig. 7d). Several smooth-profile craters were also thermally shocked without causing any apparent change.

The diameter-to-depth ratio for these craters averaged 7.62, with an average deviation of 0.38. One Martin Company crater was included in this computation because the 7.3 value compared favorably. The actual depth (of the deepest flaw or separation) divided by the depth predicted by use of the MSC glass-penetration equation is shown in Table 1. The average value is 1.99, with an average deviation of 0.07.

The crater shown in Fig. 8 was produced by the Martin Company. Because the projectiles impacting the targets were fragments of 60-μ-diam glass beads, the shapes, masses, and velocities of the projectiles were unknown. The surface views in Fig. 8 are very similar to craters caused by projectiles in the hypervelocity range, differing mainly in over-all size. The cross-sectional views (e.g., Fig. 8b) and diameter-to-depth ratios also conform to the description developed in this section (note reflected image caused by tilted target). The top surface views of some craters show a central area with extensive melting and fusion, as though impact had caused hydrodynamic flow of the glass. The lips formed on several craters have been observed to extend above the original surface of the target. The crater shown in Fig. 9 lacks the large conchoidal chip-out seen in Fig. 8. Careful sectioning (within 0.5 mm of the craters) and hand polishing revealed a cross-sectional view, a diameter-to-depth ratio of 1.3, and petaloid structures; these features conform to the criteria for low-velocity impacts.

The external surfaces of the windows of the Mercury 9 spacecraft from ten Gemini spacecraft and five Apollo command modules have been microscopically examined. These studies, yet to be published, have found at least three impacts (Figs. 10–12) which conform to the presented hypervelocity impact characteristics. In the MSC facility craters can be produced: on a light gas gun from projectiles 200 μ in diameter and larger at velocities up to 8 km/sec, and on a Van de Graaff microparticle accelerator which delivers 0.1 to 1 μ diam projectiles at velocities from 6 to 20 km/sec. Craters from these projectiles are quite similar to those found on spacecraft windows. The apparent differences in crater morphol-

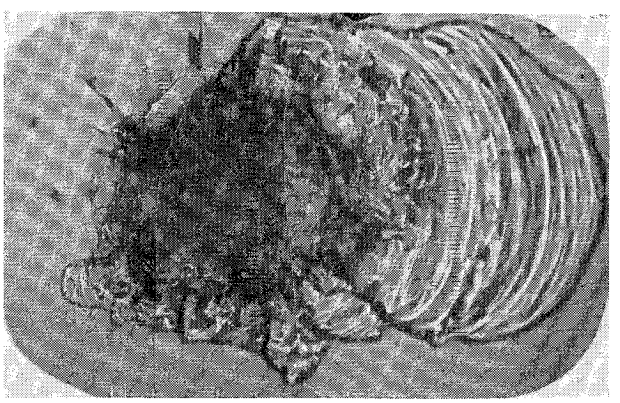

Fig. 12 Crater discovered on an Apollo 9 spacecraft window, 1.5 mm in diameter.

ogy between these craters and the developed criteria were attributed to a diameter effect, which is now being studied.

Concluding Remarks

This study has indicated that the following four criteria can be used to identify and distinguish meteoroid impacts from low-energy impact damage in fused silica: 1) the ratio of average surface diameter to the depth of the deepest fissure, 2) the percentage of the total surface area blacked-out because of total reflection, 3) the cross-sectional profile, and 4) the surface characteristics. By detailed examination of the features of craters in fused silica, one can estimate the velocity at which it was struck.

Additional studies must be performed to determine the extent to which projectile diameter and density affect the cited criteria. More data are needed in the 1.0–6.0 km/sec range, as well as at velocities in excess of 10 km/sec. Techniques must be developed to launch identical projectiles at all velocity ranges.

References

[1] Naumann, R. J., "The Near Earth Meteoroid Environment," TN D-3717, Nov. 1966, NASA.

[2] Gault, D. E. and Moore, H. J., "Scaling Relationships for Microscale to Megascale Impact Craters," TMX-54996, Feb. 1965, NASA.

MARCH 1970 J. SPACECRAFT VOL. 7, NO. 3

Stresses and Deformations in Melting Plates

EDWARD FRIEDMAN*
General Electric Company, Philadelphia, Pa.

AND

BRUNO A. BOLEY†
Cornell University, Ithaca, N. Y.

The temperature, stresses, and deformations in a melting plate are calculated. The temperature solution is obtained by means of repeated use of the concept of penetration depth with the heat balance approach. Its accuracy is measured by comparison with the results of several other solution methods. Approximate, explicit solutions for melt thickness and penetration depth are included to facilitate rapid calculations. The mechanical response is derived considering the material to be elastic-perfectly plastic with a temperature-dependent yield stress decreasing linearly to zero at the melting temperature. For a plate free of mechanical loading, elastically computed deformations are found to be fairly good upper-bound solutions to those calculated including plasticity effects. An approximate method of solution is presented for the determination of the mechanical response after peak loading is attained. The phenomenon of plastic collapse of an edge-loaded melting plate is illustrated in a sample problem.

Introduction

WHILE considerable work has been done in recent years on the calculation of melting rates and temperature distributions in melting and ablation problems,‡ comparatively little effort has been expended on analyses of the resulting thermal stresses and deformations. The investigations that have thus far been carried out in this direction include the work of Rogers and Lee,[4] concerning the viscoelastic behavior of an ablating sphere of polymethol methacrylate, Sternberg and Gurtin's[5] corresponding proof of uniqueness of solution, Weiner and Boley's[6] elastoplastic solution for stresses in a solidifying slab, Schuyler and Friedman's[7] elastoplastic treatment of an ablating heat shield structure, and Tadjbakhsh's[8] elastic dynamic analysis of the stresses in a half-space with a moving boundary. Numerous papers have been written on hollow viscoelastic cylinders with eroding inner boundaries, which relate to solid-propellant rocket motors, but thermal effects have generally been neglected.

This paper presents a general approximate method for the determination of temperatures, stresses and deformations in a melting plate. Though the design of such plates has in the past been based mainly on their primary function as heat sinks, and has, therefore, generally neglected the mechanical aspects, certain questions arise that may become important with increasing sophistication of design. Among these questions are the failure or cracking of the ablating layer, the influence of structural deformations on the aerodynamic characteristics, the possibility of using the ablating member as a part of the primary load-carrying structure, and even the eventuality of its possible repeated use in more than one mission. Clearly such matters cannot be treated without reference to the mechanical response, a treatment of which indeed forms the primary purpose of the present paper.

In order to determine an analytical solution for stresses and deformations in an ablating plate, it is first necessary to establish the temperature distribution. This is done by an approximate method, although, of course, numerous solutions of this part of the problem have appeared in the literature. The approach selected here is novel in that it repeatedly

Received July 28, 1969; revision received October 31, 1969. The results in this paper are based in part on a dissertation submitted to Columbia University. The research was sponsored by the Office of Naval Research.

* Research Engineer, Solid Mechanics Laboratory, Re-entry & Environmental Systems Division. Associate Fellow AIAA.

† Joseph P. Ripley Professor of Engineering, Department of Theoretical and Applied Mechanics.

‡ Complete bibliographies and surveys may be found in Refs. 1–3. The latter is an exposition of integral methods of analysis, which form the basis of the method employed for the temperature solution in this paper.